Nuclear Inst. and Methods in Physics Research, A 866 (2017) 172–181

Contents lists available at ScienceDirect

Nuclear Inst. and Methods in Physics Research, A

journal homepage: www.elsevier.com/locate/nima

SRF cavity alignment detection method using beam-induced HOM with curved beam orbit

Ayaka Hattori [a,*], Hitoshi Hayano [b]

[a] National Institute of Technology, Ibaraki College, 866 Nakane, Hitachinaka, Ibaraki 312-8508, Japan
[b] KEK: High Energy Accelerator Research Organization, 1-1 Oho, Tsukuba, Ibaraki 305-0801, Japan

ARTICLE INFO

Keywords:
STF accelerator
SRF cavities
Alignment
Cryomodule
HOM
Dipole mode

ABSTRACT

We have developed a method to obtain mechanical centers of nine cell superconducting radio frequency (SRF) cavities from localized dipole modes, that is one of the higher order modes (HOM) induced by low-energy beams. It is to be noted that low-energy beams, which are used as alignment probes, are easy to bend in fringe fields of accelerator cavities. The estimation of the beam passing orbit is important because only information about the beam positions measured by beam position monitors outside the cavities is available. In this case, the alignment information about the cavities can be obtained by optimizing the parameters of the acceleration components over the beam orbit simulation to consistently represent the position of the beam position monitors measured at every beam sweep. We discuss details of the orbit estimation method, and estimate the mechanical center of the localized modes through experiments performed at the STF accelerator. The mechanical center is determined as $(x, y) = (0.44 \pm 0.56\ \text{mm}, -1.95 \pm 0.40\ \text{mm})$. We also discuss the error and the applicable range of this method.

1. Introduction

Nine cell superconducting 1.3 GHz radio frequency (SRF) cavities, which are planned to be used in the International Linear Collider (ILC), are operated in a cryomodule at 2 K. In order to preserve low emittance of the accelerated beams, it is necessary to minimize long range wake fields caused by beam path offset and dispersive effects induced by inhomogeneous acceleration. To avoid these wake fields and dispersive effects, the cavity alignment has to be kept at an offset of less than 300 μm rms and a tilt of less than 300 μrad with respect to the cryomodule axis in the case of the ILC. The straightness of cavities needs to be checked and corrected before attaching the helium jackets. Since each cavity is wrapped in a liquid helium jacket and embedded inside double thermal shields in the cryomodule cryostat, it is difficult to measure the cavity alignment from outside the cryomodule without the use of expensive instruments. The alignment of the cavities within the cryomodule is precisely adjusted during assembly, using laser trackers and optical reflectors attached to the reference dips on both end beam pipe flanges. During operation, the cavities are cooled to 2 K, which consequently leads to shrinkage of all the objects within, due to thermal contraction, by roughly 1.6 mm. This thermal contraction, which might cause a deviation from the expected positioning, should be taken into consideration during the positioning and alignment of cavities.

Dipole modes comprising higher order modes (HOM) have been used to evaluate the transverse cavity alignment by exploiting the fact that the magnitude of the dipole modes is proportional to the beam transverse position. At the FreeElectron Laser in Hamburg (FLASH) in the Deutshes ElektronenSynchrotron (DESY), the beam-induced $(6/9)\pi$ mode in the first pass band (TE111-6) has been treated as a beam position monitor (BPM) and used for offset position detection, because the impedance of this mode is the largest in this pass band and the beam-induced signal is considerably strengthened and is easier to detect [1–5]. In this measurement, the beam trajectory is straight throughout the cavity, and it can be assumed that the angle wake fields are much weaker than the offset wake fields. If the beam offset is constant, then it is easy to estimate the electrical centers of the dipole modes of the cavities. In practice, the beam offset is not constant, because the beam orbit is not parallel to the longitudinal axis of the cavity. It is difficult to produce a beam orbit that is parallel to the longitudinal axis of the cavity, for which, additional analysis is required. In order to utilize dipole mode excitation by curved beam orbits, it is necessary to take particular note of the longitudinal distributions of higher order modes. The analysis, due to the wide distribution of higher order modes in the cavity excited by curved beam orbits, is complicated. On the other hand, analysis of the localized modes is less complicated, since the range of their longitudinal

* Corresponding author.
E-mail address: hattori@ece.ibaraki-ct.ac.jp (A. Hattori).

http://dx.doi.org/10.1016/j.nima.2017.05.047
Received 11 October 2016; Received in revised form 24 May 2017; Accepted 31 May 2017
Available online 15 June 2017
0168-9002/

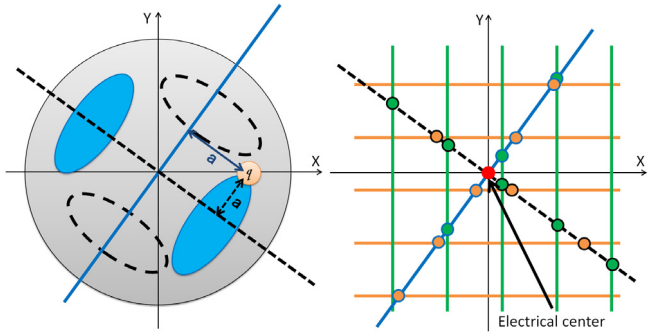

Fig. 1. The left figure shows conceptual diagram of a dipole mode cross section, where "q" denotes the position of the passing beam and the ovals indicate the electric field region of the dipole mode. Their axes are generally fixed to an angle determined by a geometrical perturbation. The right figure shows conceptual diagram of method to find electrical center. The orange lines indicate the beam sweep trajectories in x direction. The green lines indicate the beam sweep trajectories in y direction. The blue circles filled with orange and green indicate the points of minimum excitation of one polarized dipole mode in x sweeps and y sweeps respectively. The blue fitted line of the blue circles indicate the polarization axis. The black circles and dotted line are for the other polarized mode. (For interpretation of the references to color in this figure legend, the reader is referred to the web version of this article.)

distribution is narrow [6]. In this paper, we present a new analysis procedure to determine the mechanical center of a localized dipole mode excited by a curved beam orbit.

2. Basic alignment detection method

The alignment detection method is outlined below. Two characteristics of beam-induced dipole modes can be used to determine the electrical center of a cavity. The first characteristic is that their magnitudes are proportional to the beam off axis position [4]. The second characteristic is that the dipole modes split into doublets with orthogonal polarizations, with the frequency splitting caused by asymmetries due to the couplers, the antenna, and fabrication imperfections [7].

The electrical center is defined as the position where neither of the polarized dipole modes is excited by the passing beam charge. When a beam is swept in a transverse direction with an appropriate step value of the kick a, plot of the dipole mode amplitude with respect to the beam position at the location of the dipole mode takes a V-shape, and the point of minimum amplitude lies on the polarization axis. By mesh like beam step sweeps along the X and Y directions, as shown in Fig. 1, two lines that are fitted to the points of minimum amplitude are formed for one polarized dipole mode. Two minimum amplitude lines are formed because these fits are taken from the splitting of two doublet modes, i.e., two orthogonal polarizations. The intersection of these fitted lines, the mean axis of the two polarized dipole modes, indicates the electrical center of these polarized modes.

The straight beam orbits are required in this method, At the Superconducting Accelerator Test Facility (STF) accelerator, however, a curved beam orbit through two SRF cavities was observed. In this case, it appears that the low-energy beam was kicked by the RF fringe field. We demonstrate an alignment detection method with curved beam orbits using data collected at the STF accelerator. The STF accelerator was operated in 2012–2013 for inverse Compton scattering experiments in the Quantum Beam Project [8,9]. Here, an electron beam was extracted from the L band photocathode RF Gun [10], and was accelerated to 40 MeV beam energy by two 1300 MHz SRF cavities MHI-12, and MHI-13 [11,12].

The strength of the dipole mode excitation depends on the R over Q. In general a high R over Q is preferred for precision of electrical center determination. In our case, we took particular note of the distributions of higher order modes in order to utilize the dipole mode excitation by the curved beam orbit.

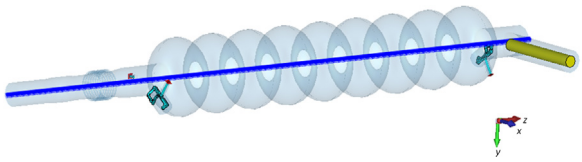

Fig. 2. SRF cavity connected to the beam pipe and bellows.

At the STF accelerator, the upstream side of cavity MHI-12 was connected to a tapered beam pipe and bellows as shown in Fig. 2, and the downstream side of it was connected to MHI-13 through a bellows. In this case, there are two modes localized in the beam pipe and the first cell whose frequencies are 2282.2 and 2309.5 MHz calculated by CST MW Studio [13]. These modes are split modes, which have different polarizations. The properties of the localized modes are described in the following section.

3. Selected localized dipole mode of SRF cavity

We calculated the transverse and longitudinal distribution of the localized dipole modes with CST MW Studio to confirm that these modes could be used for alignment detection.

The calculation was carried out with a PC, whose core processor is i7-5960X with clock speed and RAM of 3.00 GHz and 96 GB, respectively. In CST MW Studio, the cavity model is divided into 215 253 many tetrahedral meshes, and the electromagnetic fields of the meshes are solved. The solutions were obtained using a frequency domain solver, with ports, which are at the pickup antenna, and the input coupler. The calculated frequency range was from 2265 to 2465 MHz. The material within the cavity was treated as vacuum and the background material was treated as a lossy metal of conductivity 3.34×10^{19} S/m that represents electrical conductivity of Niobium at 2 K. The material of the HOM couplers and the pickup antennae were considered to be the same as the background material. The input coupler was modeled by a coaxial line. The material of the inner conductor of the input coupler was treated as a lossy metal of conductivity 5.8×10^{7} S/m that represents electrical conductivity of Copper. The transverse magnetic field H_t is set equal to zero on both the end surfaces of the entire model as the boundary condition.

3.1. Confirmation of localization by longitudinal distribution

The calculated electric fields on the longitudinal cross section at $x = 5$ mm are shown in Fig. 3. In order to show the electric fields, we took offsets at $x = 5$ mm because the magnitude of the electric fields of the dipole modes are very small in the vicinity of the mechanical center of the SRF cavity, that is, $x = 0$ mm and $y = 0$ mm. We can see that both polarized modes are localized around the upstream beam pipe. Fig. 4 shows the magnitude of the electric field distributions along the rotational symmetry axis of the beam pipe, at $x = 5$ mm and $y = 0$ mm, where z is measured from the upstream flange edge of the SRF cavity. The amplitudes of the dipole modes excited by the electron beam depend on the longitudinal component of the electric fields, E_z, along the beam orbit. The longitudinal electric fields of both polarized modes are also localized around the upstream beam pipe, as shown in Fig. 5, although the shapes of the distributions are different from those shown in Fig. 4.

3.2. Confirmation of dipole mode character by transverse distribution

Figs. 6 and 7 show the electric field of the localized modes on the transverse cross section at $z = 161$ mm, for the modes 2282.2 MHz and 2309.5 MHz respectively. Their electric field E_z at $z = 161$ mm where they have maximum sensitivity as described later, vs. the angular

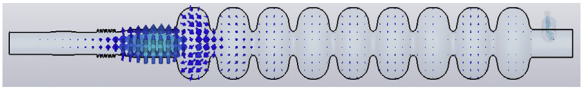

(a) 2282.2 MHz.

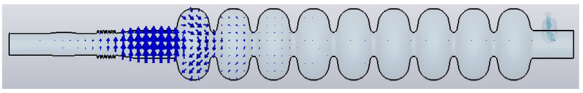

(b) 2309.5 MHz.

Fig. 3. The calculated electric fields on the longitudinal cross section at $x = 5$ mm.

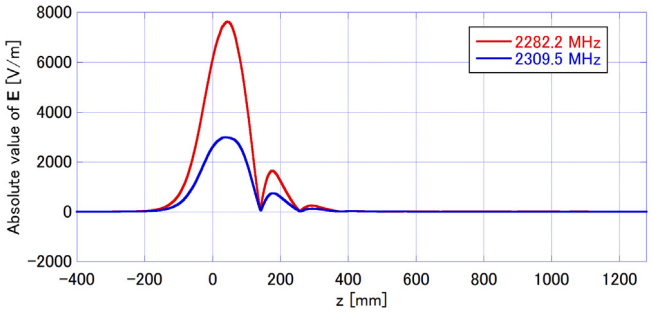

Fig. 4. The absolute value of the E distributions along the line parallel to the z axis at $x = 5$ mm and $y = 0$ mm.

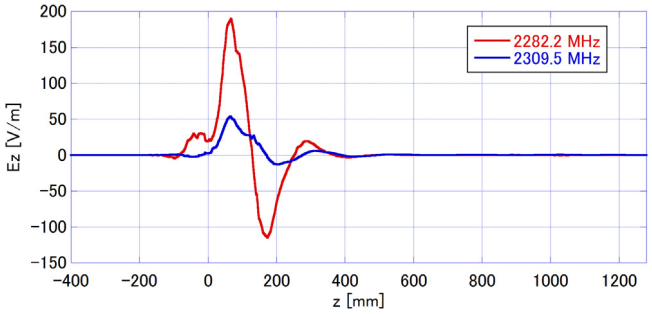

Fig. 5. E_z distribution along the z axis at $x = 5$ mm and $y = 0$ mm.

coordinate is shown in Figs. 6 and 7. These modes are dipole modes because the plots in Figs. 6 and 7 show cosine behavior.

The square of E_z distributions along the radial direction for several azimuthal angles were fitted to a quadratic function of r. Here, the SRF cavity is divided into 622 875 tetrahedra meshes for CST calculation.

In order to determine where the portion of the dipole is, we evaluate r^2 coefficients derived by the fitting the square of E_z at all values of z. The r^2 coefficient represents sensitivity of the amplitude of the dipole mode to the change of beam offset at that z position. In other words, with the same beam offsets, the change in the amplitude of the dipole mode is greater at the z position where the r^2 coefficient is greater. Fig. 8 shows the r^2 coefficients with respect to z. The r^2 coefficient of the localized mode of 2282.2 MHz is maximum at $z = 161$ mm and that of 2309.5 MHz is maximum at $z = 163$ mm.

3.3. CST calculation of electrical center

3.3.1. Electrical center considering transit time

The amplitude response of the localized modes excited by the beam after it passes through the SRF cavity has to be considered. Off axis beam excites higher order modes at all the longitudinal positions in the SRF cavities. These modes superpose and form a single wave. Therefore, their transit times have to be taken into account. Here, the SRF cavity is divided into 622 875 tetrahedra meshes for CST calculation.

We calculated $|\int E_z(r,\theta,z)\exp\{-i(2\pi f/c)z\}dz|$ for the two polarized modes on the defined lines along z axis between -400 and 1248 mm, where $r = -5,-4,\ldots,0,\ldots,4,5$, $\theta = (22.5\cdot n)^\circ, n = 0,1,\ldots,7$, f is the frequency of the localized mode, and c is the speed of light. In order to increase vertexes described later, similar calculated points with offset $(r_0,\theta_0) = (\sqrt{5}, arctan2)$ are also used. The values of $|\int E_z(r,\theta,z)\exp\{-i(2\pi f/c)z\}dz|^2$ having the same θ are plotted and fitted by a quadratic function with respect r as shown in Fig. 9, and then calculate a vertex of the quadratic function. Each vertex with different θ is converted to Cartesian coordinate. All vertexes of the quadratic functions for both polarized modes are plotted together in Fig. 10. The vertexes were excluded when they deviated by more than ±5 mm, and the correlation coefficients were less than 0. In this case, the coordinates of the vertexes were changed to the xy coordinates. Then, we fitted the positions of vertexes for each polarized mode by a linear function and found the intersection point. The intersection point was $x = -1.09 \pm 0.26$ mm and $y = 1.48 \pm 0.21$ mm. It is found that the localized modes behave as dipole modes even after integration along the z axis. Therefore, considering the contribution of the fabrication error of the HOM antenna attachment position to the error of the electrical center of the mode, the difference between the electrical center and the mechanical center was $(\Delta X_{me}, \Delta Y_{me}) = (-1.09 \pm 0.26 \pm 0.23 \text{ mm}, 1.48 \pm 0.21 \pm 0.07 \text{ mm})$.

3.3.2. Estimation of longitudinal region

Estimation of beam passing position in the localized modes is required in addition to amplitude response of dipole mode when we derive the electrical center. We considered beam passing position from a region, $z = -64.0$ to $z = 349.4$ mm, where the amplitudes of $|E_z|$ is greater than 8.8% of peak value in Fig. 11, into deriving the electrical center. 8.8% is signal noise ratio at the maximum amplitude response in this measurement.

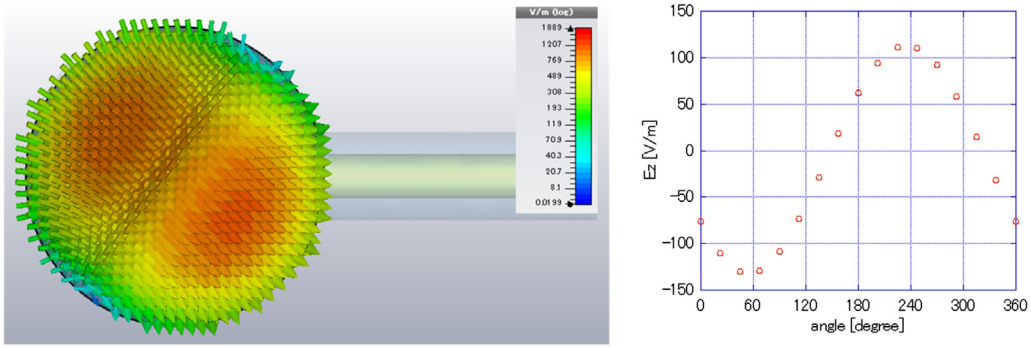

Fig. 6. The electric field $\vec{E}$ of the localized mode at 2282.2 MHz on a transverse cross section at $z = 161$ mm (left) and its angular distribution at $r = 5$ mm (right), where r is the distance from the center.

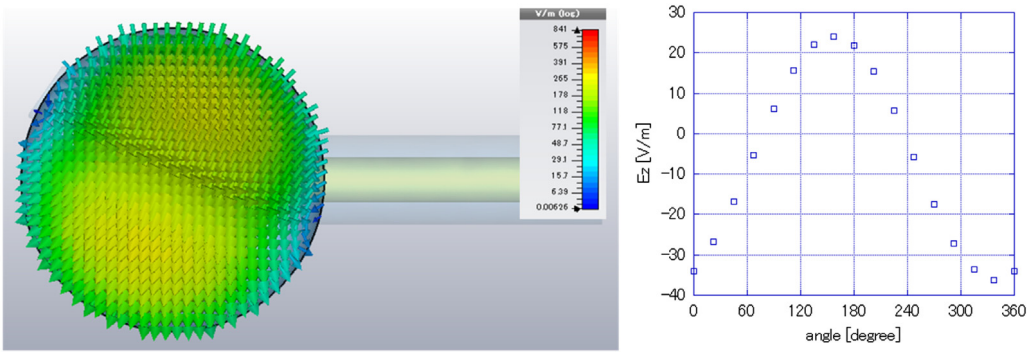

Fig. 7. The electric field $\vec{E}$ of the localized mode at 2309.5 MHz on a transverse cross section at $z = 161$ mm (left) and its angular distribution at $r = 5$ mm (right), where r is the distance from the center.

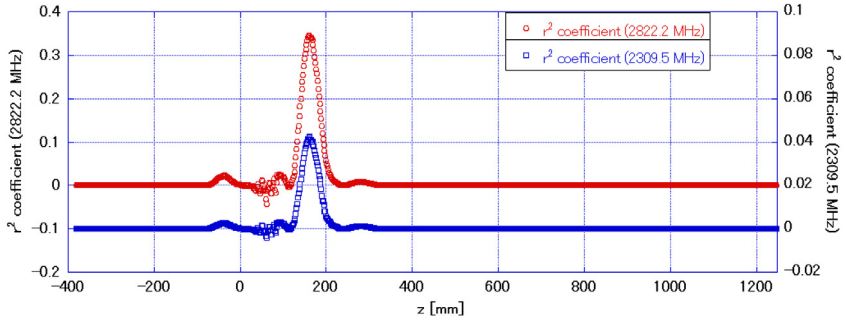

Fig. 8. The r^2 coefficient distribution along the z axis.

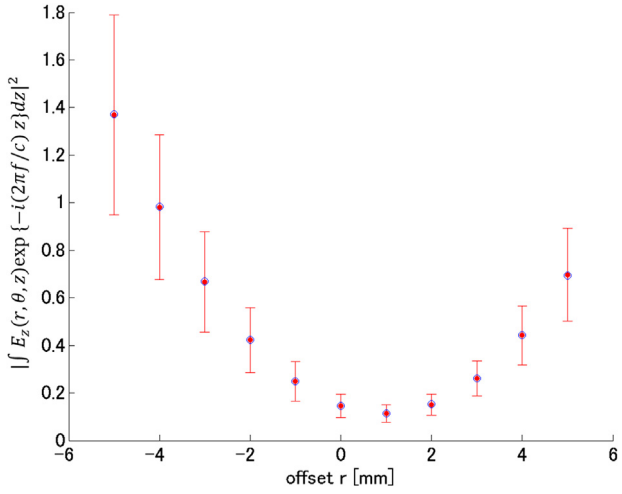

Fig. 9. The integral $|\int E_z(r,\theta,z)\exp\{-i(2\pi f/c)z\}dz|^2$ fitted to a quadratic function. The red circles are calculated values from CST MW Studio and the blue circles are obtained with the quadratic function. (For interpretation of the references to color in this figure legend, the reader is referred to the web version of this article.)

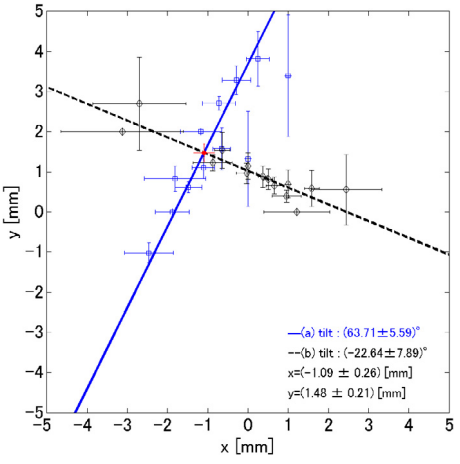

Fig. 10. The electrical center and the vertexes of the quadratic functions. The blue squares are vertexes for 2282.2 MHz and the black diamonds are vertexes for 2309.5 MHz. The red circle indicates the electrical center.

4. Electrical center estimation of localized dipole mode

We decided to use the above localized modes and estimated their electrical center excited by the electron beam at the STF accelerator.

4.1. Beam experiment

4.1.1. Cryomodule

The STF accelerator contains one capture cryomodule with two SRF cavities. This cryomodule and the alignment procedure are described below. A cross sectional view along the beam axis of the capture cryomodule is shown in Fig. 12. The capture cryomodule consists of stainless steel helium cooling pipes, two SRF cavities, and a dual aluminum heat insulating shield inside the steel vacuum chamber with a diameter of 1 m and a length of about 4 m, which is suspended by two insulation supports from the top. The upstream and downstream cavities are MHI-12 and MHI-13 respectively. An input coupler is attached to each downstream beam pipe portion of these cavities, which supplies the RF power from the room temperature side. MHI-12 was studied in this experiment.

The following describes the steps involved in the installation of the SRF cavities into the cryomodule, installation of the cryomodule into the accelerator, and the alignment procedure.

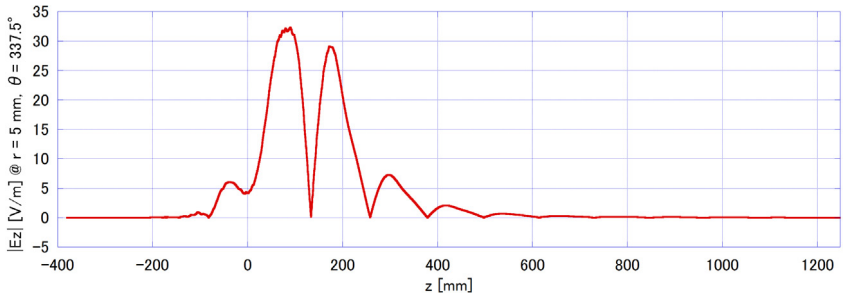

Fig. 11. The $|E_z|$ distribution for 2309.5 MHz.

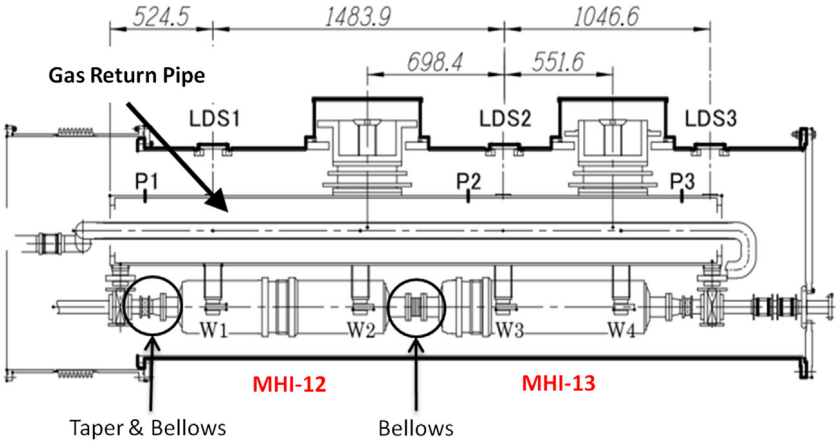

Fig. 12. The cross sectional view along the beam axis of the capture cryomodule [14].

Step 1: Cavity straightness correction and field flatness. adjustment
Step 2: Surface treatment (electropolishing, etc.).
Step 3: Vertical measurement; accelerating field test of the SRF cavities.
Step 4: Welding of the helium vessel.
Step 5: Connection of SRF cavities by rotation adjustment of the cavities in a clean room.
Step 6: Supporting from the gas return pipe.
Step 7: Alignment of SRF cavities by laser tracker with respect to reference targets on the support posts.
Step 8: Insertion of SRF cavities into the cryomodule and installation of the cryomodule into the accelerator.
Step 9: Alignment of the cryomodule using the reference target.
Step 10: Cooling to 2 K.

In Step 4, the SRF cavities are concealed in the helium vessel, and are not visible from outside. The helium vessel is welded to the SRF cavities, where it is difficult to measure the deformation due to heat of welding. The SRF cavities connected in Step 5 are moved on a rail system on the floor and suspended in the gas return pipe (Step 6). To carry out Step 7, the SRF cavities are aligned outside the cryomodule once, so that the positional relationship between the SRF cavities and the reference targets are the same when housed in the cryomodule. By using a laser tracker, the positions of the targets in each SRF cavity are adjusted to a predesigned value of the position with respect to the reference target (Step 7). The design value incorporates cooling shrinkage. To carry out Step 8, the setup is dismantled once and then incorporated into the cryostat to maintain the same positional relationship. Then, the capture cryomodule was moved into the accelerator after the cavities were inserted in it. Each cavity was equipped with the warm part of the input coupler from the side, and then the upstream and downstream cryomodule end plates were mounted. The alignment of the respective SRF cavities with respect to the cryomodule is carried out by using the above reference target as an indicator (Step 9). The alignment target holders fixed on the top surface of the heat insulating supports were used to align the cryomodule with the accelerator reference axis. Subsequent to the installation, the cavities are cooled to 2 K and the beam operation is started. The position displacement of the helium vessel during the cooling operation has been verified by a method using a wire or a reflection type laser measurement instrument. By introducing high frequency pulses of 140 MHz into the stretched ϕ70 μm gold plated tungsten wire between the capture cryomodule end plates, the position of the wire can be determined from the amplitude difference in the wire position sensor attached to the cavity, and the displacement of the cavity during cooling can be measured. Thereby, it is possible to measure the relative displacement of the cavity. The vertical displacement of the upper surface of the gas return pipe can be indirectly measured by using reflection-type laser position detector. The wire position sensors, W1 and W2 on MHI-12, and W3 and W4 on MHI-13, were attached to the upstream and downstream portions of the SRF cavities. Since the displacement obtained is a relative value based on the position before the cooling operation, it is impossible to evaluate the alignment without the assumption that the alignment in Step 7 is also maintained after Step 9. The displacement in the helium vessel also cannot be evaluated because the SRF cavities in Step 4 are concealed in the helium vessel as previously described. In this respect, the alignment detection using beam-induced localized modes has the advantage that it can evaluate electrical center of the SRF cavities.

Before installation of the two cavities in the cryostat in Step 7, the measured deviations from the reference value were within the range from −0.1 mm to +0.15 mm in the x direction and from 0 mm to +0.2 mm in the y direction.

Displacements at 2 K with respect to the values at room temperature measured by each sensor are shown in Table 1 [14].

According to this measurement and considering uniform thermal contractions amount due to cooling, 0.4 and 1.57 mm in x, y direction, the average offsets of the MHI-12 used in this study were −0.09 mm in the x direction and 0 mm in the y direction, and the tilts were

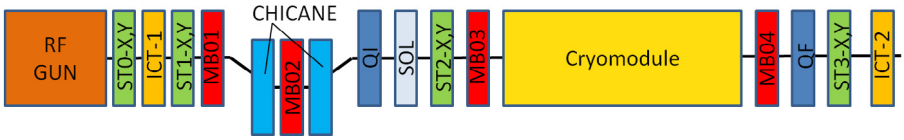

Fig. 13. The conceptual view of the beam line setup.

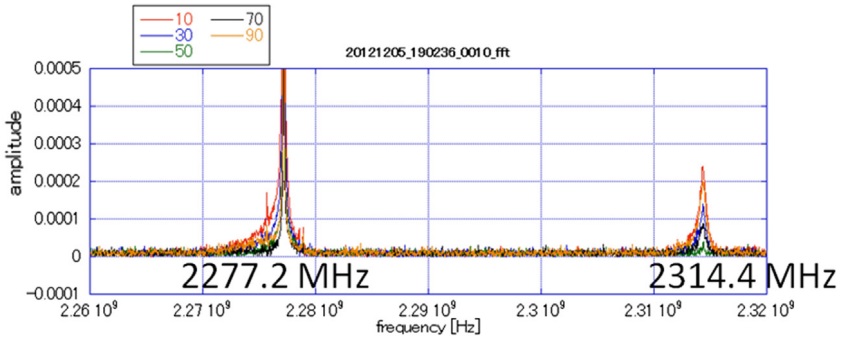

Fig. 14. The spectra of HOM signal excited by the electron beam. The traces with different colors show the signal with different beam sweep angle. (For interpretation of the references to color in this figure legend, the reader is referred to the web version of this article.)

Table 1
Displacements at 2 K with respect the values at room temperature measured by the wire position sensors.

	X displacement [mm]	Y displacement [mm]
W1	−0.35	−1.60
W2	0.25	−1.72
W3	−0.10	−1.72
W4	−0.25	−1.66

0.8 mrad in the x direction and −0.16 mrad in the y direction with respect to the position of the cavities aligned at room temperature. However, the position of cavities at the beginning of the cooling operation was unknown, since the deviation due to installation work after alignment of the cavity was unclear. Therefore, the absolute values of the displacements remain unknown.

4.1.2. Accelerator beam line setup

The detection of the localized dipole modes, which were excited by the electron beam, was performed in the STF accelerator. The conceptual view of the STF accelerator beam line setup is shown in Fig. 13.

The normal conducting L-band RF electron gun (RF gun) [15,16] using a Cs_2Te photocathode as an ultra-low emittance electron beam source was used. The beam energy out of the RF gun was estimated 4.01 MeV. A chicane was located downstream of the RF gun to measure the electron beam energy. A quadrupole magnet and a solenoid magnet were located downstream of the chicane. The beam parameters used in this measurement were: 28 bunches with a ~50 pC/bunch charge, 6.15 ns bunch spacing, and a 5 Hz repetition rate.

The accelerating electric fields of MHI-12 and MHI-13, which were calculated based on the assumption that electrons travel close to the speed of light, were set to 16 MV/m and 24 MV/m corresponding to 22.6 and 33.9 MV/m peak electric fields respectively.

Two corrector magnets ST2-X and ST2-Y, which were positioned upstream of the cryomodule, were used to shift the transverse beam position in the SRF cavities, for measurement of the response of the beam-induced HOMs. ST2-X and ST2-Y can kick the beam in the x direction (horizontal axis) and the y direction (vertical axis) respectively. Two beam position monitors, MB03 and MB04, located upstream and downstream of the cryomodule respectively, were also used. Further, the beam intensity monitors ICT-01 and ICT-02 were located upstream and downstream of the cryomodule respectively.

4.2. Measurement of HOM

Between the two SRF cavities installed in the capture cryomodule, only the upstream cavity (MHI-12) is used for HOM detection and analysis in this work. MHI-12 has two HOM couplers in both the end beam pipes. The input coupler is located in the downstream end beam pipe.

Approximately 25 m long coaxial cables were connected between the HOM couplers and the front end electronics before an oscilloscope (Agilent Technologies DSO9404A). For the front end electronics, three high pass filters (HPF, Mini Circuits VHF-1500+), and a HPF (2100) were used to select the localized dipole mode in the HOM. In order to synchronize the passing beam with its induced HOM signals obtained by the oscilloscope (with 10 G samples/s and 262 k points in one acquisition with 8 bit resolution), two BPM signals with the same passing beam and induced HOM signals were taken simultaneously during 10 transverse beam sweeps, which include 5 horizontal direction sweeps and 5 vertical direction sweeps. A baseline clipping circuit and average signal over 28 bunches were used in the BPM electronics. The signal charge integration gate width of the ICTs was 30 ns, so that 5 bunch signals were captured because the bunch interval was 6.15 ns. Using the two BPM data sets, we estimated beam position in the beam pipe. Nonlinear corrections to response of the clipping circuits and inherent nonlinearity in the position calculations are required to estimate the beam positions. By measuring the circuit response curves due to change in the input signal intensity, using a raw BPM signal, and simulated beam position response by the HFSS code [17], the beam positions were corrected. The frequencies of the detected modes were 2277.2 and 2314.4 MHz as shown in Fig. 14. The different curves show the spectra with different beam sweep angle and number of them indicates serial numbers of acquired data. As the number increases, the beam sweep angle decreases and then increases. The response of peak amplitudes of spectra with the beam sweep can be seen in Fig. 14. Both localized modes were detected from signals of the upstream HOM coupler.

4.3. Estimation of electrical center

There are two stages for estimating the electrical center after data collection. One is reconstruction of the beam orbit and the other is calculation of the electrical center. Fig. 15 shows the flowchart of the analysis. The details of the stages are described in the following sections. The electrical center is required to satisfy two criteria: the summation

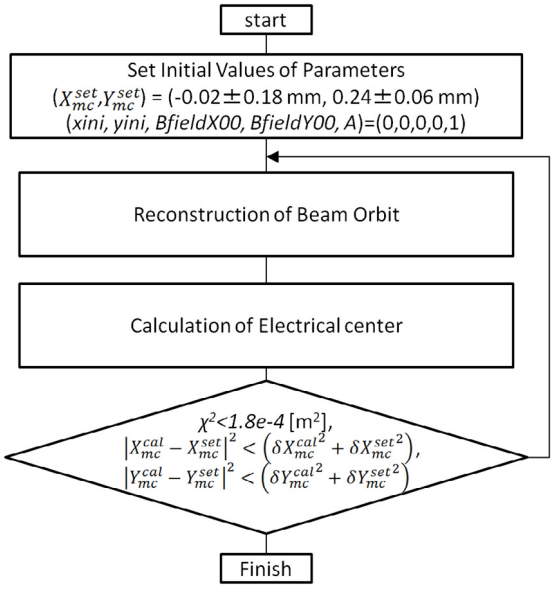

Fig. 15. Flowchart for estimating the electrical center.

of the squared difference between the calculated beam positions and the measured beam positions at MB03 and MB04 for the all sets, $\chi^2 < 1.8 \times 10^{-4}$ m^2, which is related to the quality of reconstruction of the beam orbit, and the difference between the calculated mechanical center and the set mechanical center should be within acceptable range of error.

4.4. Reconstruction of the beam orbit by GPT

When the x coordinate of the beam position was displaced in the positive direction at MB03 by increasing the current in ST2X, it was found to be displaced in the negative direction at MB04. Therefore, the beam did not move linearly between the two BPMs. Hence, beam simulation was carried out in order to calculate the beam passing position from downstream of the chicane to MB04 by using the General Particle Tracer (GPT) package [18].

4.4.1. Modeling for orbit calculation

A model for calculating the orbit is shown in Fig. 16. The model consists of a constant electric field bounded by a rectangular box for modeling the beam energy downstream of the chicane, four corrector magnets, ST-00X, ST-00Y, ST-02X and ST-02Y, a quadrupole magnet (QI), a solenoid (SOL), and RF fields of the two SRF cavities.

The initial electron beam including 100 particles is generated at $z = 0$ and its charge is 50 pC. The electron beam offsets, x_{ini} and y_{ini} at $z = 0$ in x and y directions were parameterized. Also, the electron beam tilts were adjusted by changing the magnitudes of magnetic fields, BfieldX00 and BfieldY00, produced by ST00-X and ST00-Y. The initial electron beam energy is fixed at 0.4 eV and accelerated to 4.01 MeV by a constant electric field of 200 MV/m. For MHI-12 and MHI-13, we set the electric fields corresponding to peak electric fields of 22.6 and 33.9 MV/m. The phase difference between MHI-12 and MHI-13 was fixed at 90° and the phase of MHI-12 was set to the phase corresponding to the maximum acceleration acquired by the beam in the experiment. In order to account for error in the measurement of electric field estimated from a value of a RF power meter, we have introduced a correction factor A. The tilts and offsets of the SRF cavities were set to the values estimated from the data by the laser tracker and the wire position sensors. However, only the offsets of MHI-12 were treated as parameters in the GPT calculation.

The upstream edge of the quadrupole magnet of length 0.1 m was positioned at $z = 0.125$. We set the magnetic field gradient to 0.054 T/m as the inspection report by the manufacturer. In order to account for the fringe field, the magnetic fields of the corrector magnets, ST2-X and ST2-Y, were modeled by 17 rectangular subdivided magnets of length 10 mm. The magnetic field strength can be written as a product of the current and a conversion factor, which is determined by the magnetic field measurement of the corrector magnets.

4.4.2. Reduction of χ^2

We calculated the beam orbits with GPT based on 10 transverse beam sweeps. The beam position χ^2 was calculated as the summation of the squared difference between the calculated beam positions and the measured beam positions at MB03 and MB04 for the all sets. However, the data was ignored when the measured beam position was outside the BPM range (−6.5 mm, 6.5 mm). The target χ^2 was set to 1.8×10^4 m^2 decided from the accuracy of the alignment and fluctuations of beam positions; the following parameters were varied: x_{ini}, y_{ini}, BfieldX00, BfieldY00 and A, where A is a correction factor defined in Section 4.4.1. Fig. 17 shows an example of an orbit sweep for one set, described above, by carrying out the procedure shown in Fig. 15. The marks '+' and 'x' indicate the calculated and measured beam positions at MB03 and MB04 respectively with different dipole magnet current for an orbit sweep. MB03X and MB03Y mean x position at MB03 and y position at MB03. Similarly, MB04X and MB04Y are also x, y positions at MB04. Examples of calculated beam orbits from $z = 0$ to MB04 are shown in Fig. 18. In Fig. 18(a) and (b), the curves show x and y position respectively along z position with different dipole magnet currents for an orbit sweep in the x direction. In Fig. 18(c) and (d), the curves show x, y position along z position for an orbit sweep in the y direction. It can be seen from Fig. 17 that the calculated beam positions fit well to the measured beam positions. The divergence of the spread due to ST2-X and ST2-Y changes at the entrance of the upstream of the SRF cavity. The longitudinal center of the localized modes is positioned on the vertical red line near the entrance of the upstream SRF cavity as shown in Fig. 18.

4.5. Calculation of electrical center

There are two steps to calculate the electrical center. First, we need to know dipole magnet currents when the beam passes through the electrical center of the localized mode. Second, we calculate beam orbits from $z = -64.0$ to 349.4 mm.

4.5.1. Response of localized mode to beam sweep

In order to derive the dipole magnets when beam passes through the electrical center of localized modes, the response with beam sweep is examined. The procedure is described in the following. The amplitude, y, normalized with beam charge can be fitted by the following function

$$y = |ax + b| + c,$$

where, x is the dipole magnet current, a and b are fitting parameters and c is related to the noise level. However, the fitting range is important and required. Therefore, we consider obtaining the dipole magnet currents for which the beam passes through the electrical center of the localized mode by fitting the square of these normalized amplitudes.

First, we find the symmetry axis in order to estimate c. Although $(|ax + b| + c)^2$ is not a quadratic function, we can find the axis by fitting the squared equation by a quadratic function. We define c as the average of y around $x = -b/a$ symmetry axis. The amplitude y is averaged over the range where the average value $\langle y \rangle$ is close to the y values around the symmetry axis. Using this value of c, we fit

$$Y = (y - c)^2 = (ax + b)^2$$

using a quadratic function. Here $(y - c)^2 = ax^2 + 2abx + b^2$ can be fitted to a quadratic function. In this case, let the error be the deviation σ of c. Furthermore x, where $(y - c)^2$ attains the minimum value, was calculated. Using the value of x obtained here, the mapping plot was created as shown in Fig. 19. We use the average value for the coordinates

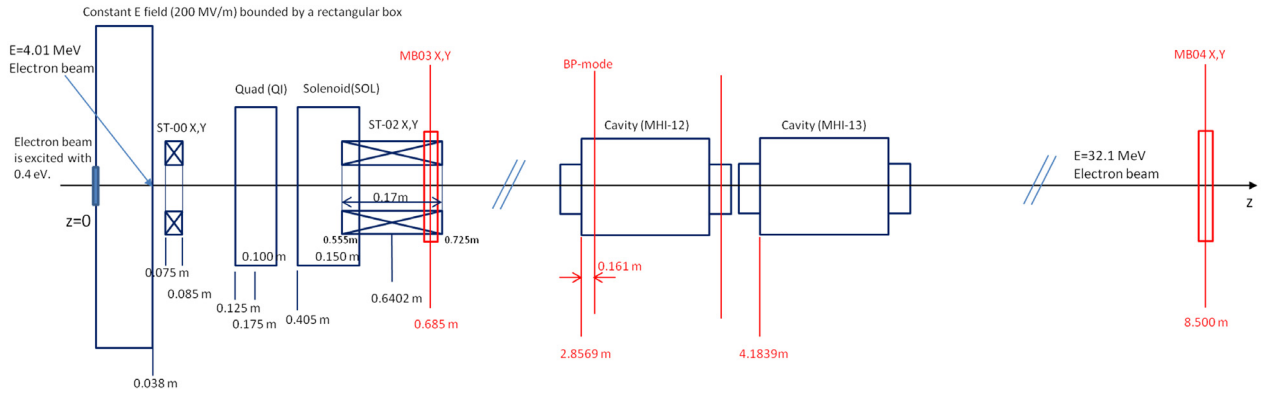

Fig. 16. Model for calculation of the beam orbit.

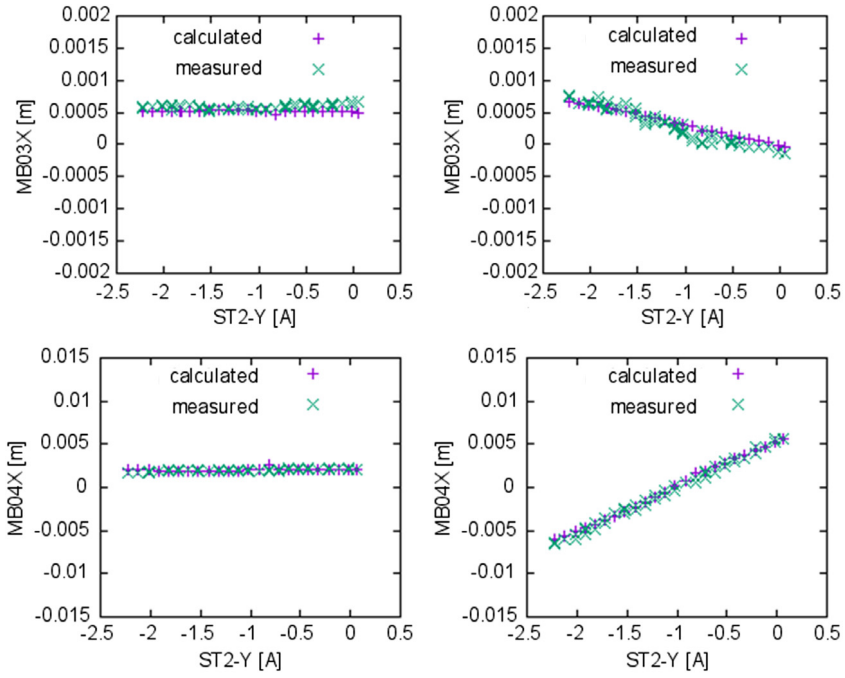

Fig. 17. An example of the orbit sweep for one set. '+' indicates the calculated data and 'x' indicates the measured data.

in the direction where beam sweep was not carried out. Then the dipole magnets current when the beam passes through the electrical center of localized modes are 1.000 ± 0.002 A in x and -1.485 ± 0.002 A in y by fitting two minimum amplitude lines and calculating the intersection of these. The above method was applied to the acquired data of the localized modes, with the following two conditions:

(1) The differences between the measurements of ICT-01 and ICT-02 must be less than 2 pC.

(2) The amplitude of each BPM electrode must be in the range of an analog to digital converter

4.5.2. Region of mechanical center of the localized modes

The region where the electrical center is, $\left(X_{ec} \pm \delta X_{ec}, Y_{ec} \pm \delta Y_{ec}\right)$, was determined as the region from the maximum value to the minimum value of beam orbit from $z = -64.0$ to 349.4 mm with the dipole magnet currents when the beam passes through the electrical center of the localized modes, described in the previous section. The mechanical center, $\left(X_{mc}^{cal}, Y_{mc}^{cal}\right)$, can be calculated by subtracting the difference between the electrical center and the mechanical center described in Section 3.3.1, $\left(\Delta X_{me}, \Delta Y_{me}\right) = (-1.09 \pm 0.26 \pm 0.23 \text{ mm}, 1.48 \pm 0.21 \pm 0.07 \text{ mm})$, from the derived electrical center, as shown in the following equation.

$$P_{mc}^{cal} = P_{ec} - \Delta P_{me}, \quad P = X, Y$$

4.5.3. Reduction of difference between calculated mechanical center and set electrical center

After calculation of the mechanical center, we examined whether the derived electrical center agrees with the mechanical center set in the GPT package. Therefore, we calculated the quantity,

$$\left|P_{mc}^{cal} - P_{mc}^{set}\right|^2 - \left(\delta P_{mc}^{cal\,2} + \delta P_{mc}^{set\,2}\right), \quad P = X, Y.$$

When the squared difference $\left|P_{mc}^{cal} - P_{mc}^{set}\right|^2$, is greater than the summation of the squared errors, $\delta P_{mc}^{cal\,2} + \delta P_{mc}^{set\,2}$, we changed the offsets of MHI-12 set in GPT package and repeated the reconstruction of the beam orbit and calculation of electrical center until the squared difference becomes less than the summation of squared errors. The history of reduction of difference between calculated and set electrical center is shown in Fig. 20.

4.5.4. Electrical center

The calculated mechanical center is moved by change of the set mechanical center. Fig. 21 shows $\left|P_{mc}^{cal} - P_{mc}^{set}\right|^2 - \left(\delta P_{mc}^{cal\,2} + \delta P_{mc}^{set\,2}\right)$ with respect to the calculated mechanical center. When $\left|P_{mc}^{cal} - P_{mc}^{set}\right|^2 - \left(\delta P_{mc}^{cal\,2} + \delta P_{mc}^{set\,2}\right)$ is less than 0, that is the region of mechanical center,

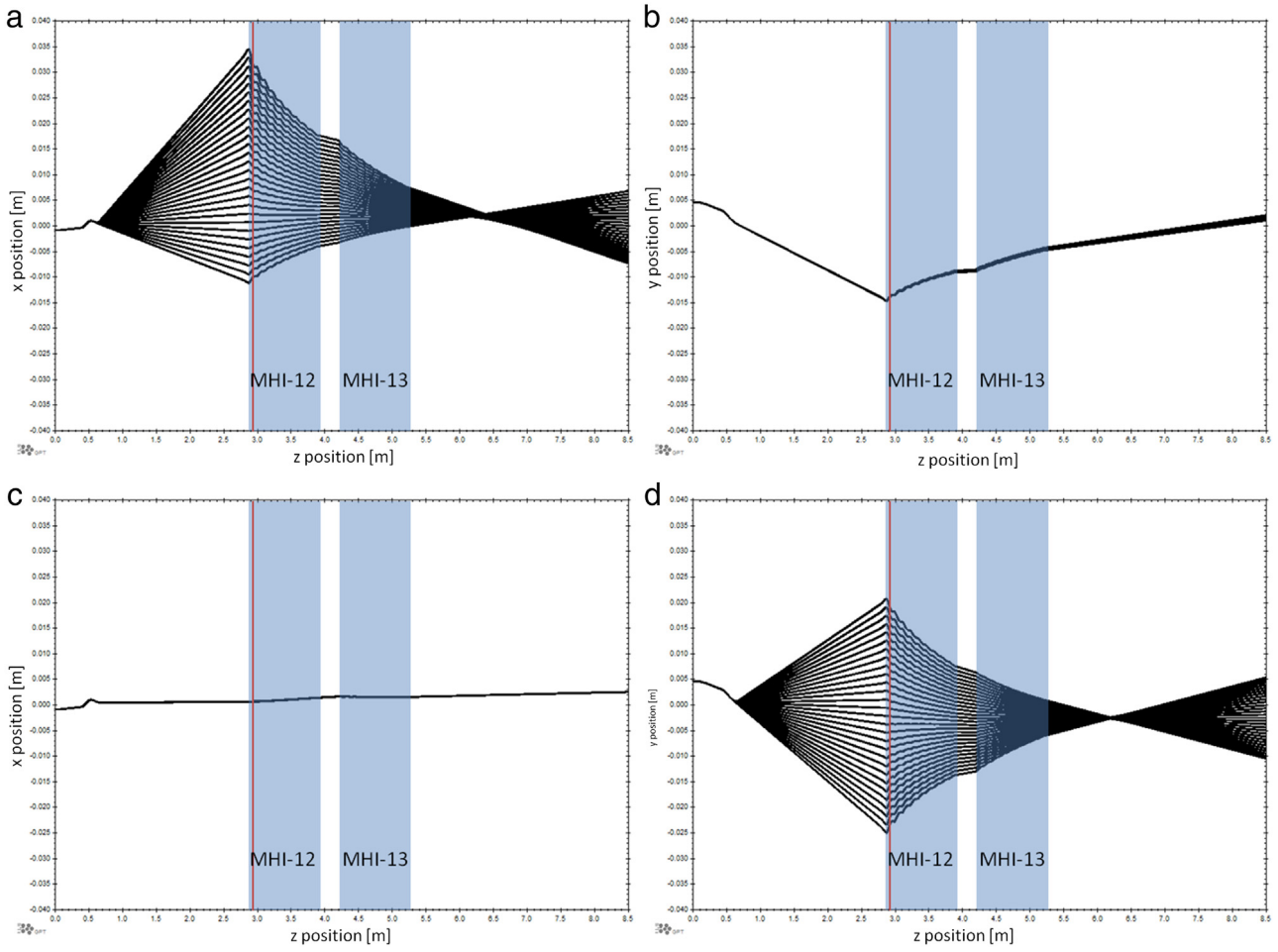

Fig. 18. Examples of calculated beam orbits. (a) and (b) show the beam orbits for beam sweep in the x direction. (c) and (d) show the beam orbits for beam sweep in the y direction.

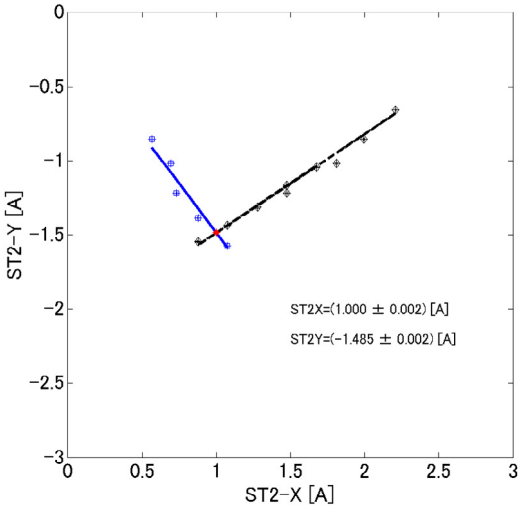

Fig. 19. The mapping plot of dipole magnet currents at the minimum amplitude.

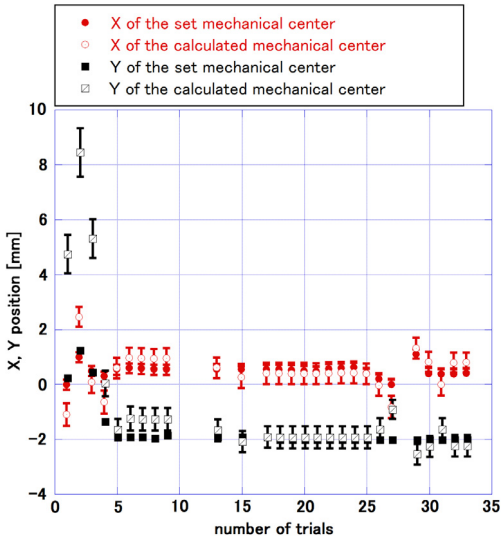

Fig. 20. The history of reduction of difference between calculated mechanical center and set electrical center.

$(x, y) = (0.44 \pm 0.56\ \text{mm}, -1.95 \pm 0.40\ \text{mm})$, satisfies the two criteria described in Section 4.3.

The final values of the GPT parameters are given in Table 2.

5. Discussion

The tilts (x-tilt and y-tilt) of MHI-12 and the offsets (x-offset and y-offset) and tilts of MHI-13 were fixed in the calculation. The reason why

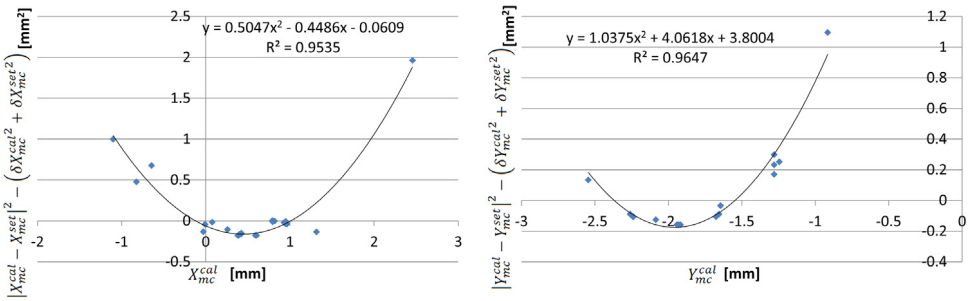

Fig. 21. $|P_{mc}^{cal} - P_{mc}^{set}|^2 - \left(\delta P_{mc}^{cal2} + \delta P_{mc}^{set2}\right)$ with respect to the calculated mechanical center.

Table 2
Final values of the GPT parameters.

Parameters	Final values
x_{ini}	−0.2 mm
y_{ini}	4.96 mm
BfieldX00	0.6 mT
BfieldY00	4.3 mT
A	0.90

these were fixed for MHI-13 is that the beam orbits are less influenced there due to the higher energy. The reason why the tilts of MHI-12 were fixed is that we expect that the influence of the tilts is small because the estimation error of the uniform thermal contraction amount due to cooling, which influences mainly the offset, is considered to be large. The offsets of MHI-12 were variable parameters.

We investigated the influence on the mechanical center when these fixed parameters deviated from the initial alignment values with errors. Expected errors from the alignment accuracy are estimated to be 0.1 mm for offset and 0.2 mrad for tilt. When the tilt of MHI-12 is changed by 0.2 mrad, the mechanical center changes to $(x, y) = (0.82 \pm 0.36\ \text{mm}, -2.26 \pm 0.38\ \text{mm})$ when the orbits can be reconstructed and the calculated mechanical center and the set mechanical center agree with each other within the errors range. Similarly, when the offset of MHI-13 is changed by 0.1 mm, the mechanical center changed to $(x, y) = (-0.01 \pm 0.40\ \text{mm}, -1.64 \pm 0.41\ \text{mm})$. When the tilt of MHI-13 is changed by 0.2 mrad, the mechanical center changes to $(x, y) = (0.80 \pm 0.37\ \text{mm}, -2.24 \pm 0.39\ \text{mm})$. All changes of the mechanical center are within the error range of the result obtained by this analysis.

At the STF accelerator, there is no localized mode, which would be useful for alignment detection, in the downstream beam pipe of the cavity due to existence of input coupler. However, we expect that the full determination of the cavity offset and tilt is realizable by putting more BPMs upstream and downstream of one cavity to measure beam trajectory precisely and using one more localized mode.

We summarize our method of obtaining the mechanical center in the following steps. This method is applicable if the localized modes exist regardless whether cavity is superconducting or not.
(1) Carry out amplitude measurement of the localized mode during beam sweep.
(2) Reconstruct beam orbit using beam position monitor data by GPT.
(3) Calculate electrical center using (1) and (2).
(4) Determine the accelerator parameters by repeating (2) and (3) until the condition of χ^2 and calculated mechanical center deviation from the set mechanical center are satisfied as shown in Fig. 15.

6. Conclusion

We have developed a method for determining the mechanical center of the localized modes, even for beam energies so low that the beam can be kicked by the RF fringe field. In the case of similar studies [1–7], beam trajectories were used which could be regarded as straight. It is for the first time that beams with curved orbits are used to induce dipole modes in order to estimate the electrical center. In this case, estimation of beam orbits, and the longitudinal distribution of dipole modes are required. We estimated the electrical center of the localized mode by estimating the beam orbit using the GPT package and by calculating the longitudinal distribution of localized dipole modes using the CST package. The mechanical center determined by this method for the localized modes in the nine cell superconducting cavity was $(x, y) = (0.44 \pm 0.56\ \text{mm}, -1.95 \pm 0.40\ \text{mm})$.

Acknowledgments

The authors would like to thank all the members of the STF group and the group of the Quantum Beam Technology Program for their support in the accelerator construction, operation and their cooperation on this study. The work was supported by the Quantum Beam Technology Program of the Japanese Ministry of Education, Culture, Sports, Science, and Technology (MEXT). The work was supported by JSPS KAKENHI Grant Number JP26400300. The work was also supported by the graduate University for Advanced Studies, SOKENDAI.

References

[1] N. Baboi, G. Kreps, G. Devanz, O. Napoly, R.G. Paparella, Preliminary Study on HOM-based Beam Alignment in the TESLA Test Facility, in: Proceedings of LINAC2004, Lubeck, Germany, 2004, pp. 117–119.
[2] M. Ross, et al., Cavity Alignment Using Beam Induced Higher Order Modes Signals in the TTF Linac, in: Proceedings of 2005 Particle Accelerator Conference, Knoxville, Tennessee, 2005, pp. 2284–2286.
[3] S. Pei, Z. Li, K. Bane, J. Smith, TTF HOM Data Analysis with Curve Fitting Method, in: Proceedings of EPAC2008, Genoa, Italy, 2008, pp. 1227–1229.
[4] S. Molloy, et al., High precision superconducting cavity diagnostics with higher order mode measurements, Phys. Rev. ST Accel. Beams 9 (2006) 112802.
[5] K. Watanabe, The Graduate University for Advanced Studies (SOKENDAI), (Ph.D. thesis). 2008, http://ci.nii.ac.jp/naid/500000446916.
[6] P. Zhang, Beam Diagnostics in Superconducting Accelerating Cavities, Springer International Publishing, Switzerland, 2013.
[7] S. Molloy, High Precision SC Cavity alignment Measurements with Higher Order Modes, SLAC-PUB-12349, Care-Report-2006-SRF, 2007.
[8] J. Urakawa, J. Phys. Conf. Ser. 357 (2012) 012035-1.
[9] H. Shimizu, et al., Nucl. Instrum. Methods A 772 (2015) 26–33.
[10] M. Kuriki, et al., Japan. J. Appl. Phys. 52 (2013) 056401-7.
[11] Y. Yamamoto, et al., Nucl. Instrum. Methods A 729 (2013) 589–595.
[12] M. Omet, et al., Development and Test of a Fully Automated PkQl Control Procedure at KEK STF, in: Proceedings of IPAC2013, Shanghai, China, 2013, pp. 2950–2952.
[13] CST MICROWAVE STUDIO®, © 2015 CST Computer Simulation Technology AG. [Online]. Available: https://www.cst.com/Products/CSTMWS.
[14] K. Tsuchiya, et al., Capture cavity cryomodule for quantum beam experiment at KEK superconducting RF test facility, AIP Conf. Proc. 1573 (2014) 803.
[15] J. Baehr, et al., Behavior of the TTF2 RF Gun with long pulses and high repetition rates, TESLA Note (2003) 2003–2033.
[16] S. Kashiwagi et al., Development of a Photocatode RF Gun for the L-band Linac at ISIR, in: Proceedings of IPAC2010, Kyoto, Japan, 1728–1730, 2010.
[17] ANSYS HFSS, ANSYS HFSS website, [Online]. Available: http://www.ansys.com/Products/Simulation+Technology/Electronics/Signal+Integrity/ANSYS+HFSS.
[18] AET, INC., http://www.aetjapan.com/english/software.php?Accelerators_Design=GPT, 2016. [Online].